Modeling Gas Diffusion Layers in Polymer Electrolyte Fuel Cells Using a Continuum-based Pore-network Formulation

P.A. García-Salaberri[a,b], I.V. Zenyuk[c], J.T. Gostick[d], A.Z. Weber[b]

[a] Departamento de Ingeniería Térmica y de Fluidos, Universidad Carlos III de Madrid, Leganés, 28911, Spain
[b] Energy Conversion Group, Lawrence Berkeley National Laboratory, Berkeley, CA 94720, USA
[c] Department of Chemical Engineering and Material Science, National Fuel Cell Research Center, University of California, Irvine, CA 92697, USA
[d] Department of Chemical Engineering, University of Waterloo, Waterloo, ON N2L3G1, Canada

Multiscale modeling of porous media in polymer electrolyte fuel cells is of paramount importance to improve predictions and assist the design of new materials. In this work, a composite-continuum-network formulation is presented to model species diffusion and convection in gas diffusion layers (GDLs). The model can be incorporated into CFD codes with moderate computational cost. The macroscopic model is based on a structured mesh composed of parallelepiped control volumes (CVs) and differential connectors (with negligible volume). The CV mesh embeds an internal structured pore network, which is used to determine analytically local anisotropic effective transport properties (effective diffusivity and permeability). The global structural parameters and effective transport properties predicted by the model are in good agreement with previous experimental data. Moreover, the results show that heterogeneities in the GDL can have significant influence on the fluxes from/to the catalyst layer, thus affecting local degradation rates.

Introduction

Polymer electrolyte fuel cells (PEFCs) are promising power sources for stationary, portable and vehicular applications due to its unique advantages, including quiet operation, quick start-up and load response, and high efficiency (1). In the last decades, several fuel cell vehicles have been developed by automakers, such as General Motors, Hyundai and Toyota. However, the widespread commercialization of PEM fuel cells for vehicular applications is still limited by their cost, performance and durability, among which durability is the most challenging aspect (2). The target lifetimes for PEFCs set by the U.S. Department of Energy (DOE) are 5,000 h for passenger cars, 25,000 h for transit buses, and 40,000 h for stationary applications (3). Therefore, currently there is an urgent need to demonstrate these lifetimes, while decreasing capital and operating costs.

Many works can be found in the literature that purpose new materials to increase durability of catalyst layers, membrane, gas diffusion layers (GDLs), and bipolar plates (see, e.g., (4) and references therein). However, there is still a need of understanding about the mechanisms and the effect of operating conditions on the overall durability of PEFCs. An example is the corrosion of the carbon support in the cathode catalyst layer due to hydrogen starvation, and how the local blockage created by liquid water affects this process (5).

In this context, mathematical modeling is an indispensable tool to analyze PEFC performance and degradation, and to examine the impact of material microstructure on the macroscopic response of the system. Inevitably, this task requires the development of multiscale models that incorporate key information from the microscale into the macroscale, while keeping computational cost moderate for engineering applications (6-8). In the last years, models with increasing level of complexity have been developed to gain insight into the effect of heterogeneities on cell performance (9-15) but it is missing a flexible modeling framework that can be widely adopted in CFD macroscopic models (16).

With this aim, in this work a macroscopic model of a GDL that incorporates the effect of microstructural heterogeneities using a control volume (CV) mesh is presented. The CV mesh embeds an internal pore network (PN), which is used to determine analytically local anisotropic effective transport properties at the macroscopic scale. Species diffusion and convection are examined. The organization of the paper is as follows. First, the generation of the CV mesh at the macroscopic scale is presented. Then, the PN embedded in the CV mesh is described. Subsequently, the formulation used to determine analytically the local effective transport properties based on the PN, as well as the simulations used to determine the global effective properties in the CV mesh, are presented. Next, the results are discussed with a focus on the effect of heterogeneities on spatial distributions and local fluxes. Finally, the concluding remarks are summarized.

Control Volume Mesh

As shown in Figure 1, the GDL domain is divided into two types of constructive elements: CVs and differential connectors (with exceedingly small volume). The two elements form a structured CV mesh, so the parallelepiped CVs are connected through parallelepiped connectors on each face. The connectors in perpendicular directions are separated by small solid zones (walls). Both the CVs and the connectors are meshed with 27 computational cells ($3 \times 3 \times 3$). The characteristic size of the CVs is set to $L_x = L_z = 60\ \mu$m in the material plane (x-z plane) and $L_y = 30\ \mu$m in the through-plane direction (y-direction). These characteristic sizes provided a good measure for the uncompressed Toray carbon paper examined here but can be adapted depending on the compression ratio and the GDL fabric (9,17,18). The model was implemented in the finite volume code ANSYS Fluent, although it could also be used in other CFD codes, such as COMSOL Multiphysics.

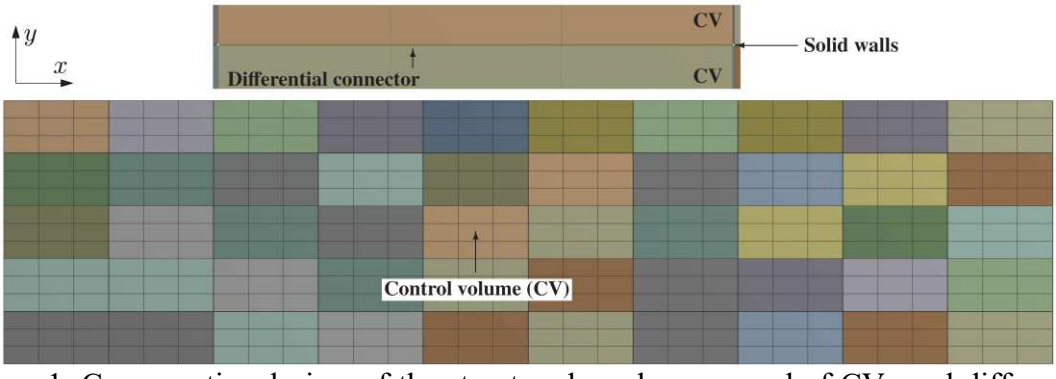

Figure 1. Cross-sectional view of the structured mesh composed of CVs and differential connectors. Each constructive element is meshed with $3 \times 3 \times 3$ computational cells. The close-up view shows a differential connector between two CVs. The connectors in perpendicular directions are separated by small solid zones.

Structured Pore Network

A structured PN is embedded into the CV mesh, so that each CV includes one pore in the center of the CV and the corresponding six throats (two in each direction, $t1$ and $t2$). Each differential connector includes a differential slice of throat, which is useful to simulate invasion percolation in the CV mesh, an aspect that will be addressed in future work. Here, the PN is used to extract local effective transport properties in the CVs and connectors, as discussed later. The generation of the PN and calculation of effective properties was implemented in MATLAB.

The geometry of the PN in a CV is shown in Figure 2. The characteristic sizes of the pores in each direction ($L_{p,x}$, $L_{p,y}$ and $L_{p,z}$) are prescribed according to the cumulative pore size distribution (CPSD) of the GDL. Here, we used the CPSD determined by Zenyuk et al. (18) using X-ray computed tomography for 20 wt% PTFE-treated uncompressed Toray TGP-H-120. The geometry of the throats in a CV is defined by its length in each direction ($L_{t,x}$, $L_{t,y}$ and $L_{t,z}$), and the half-height, $H_{t,i}$, and half-width, $W_{t,i}$, of its cross-sectional area (note that the subscript i indicates the along-the-throat direction, i.e., the direction perpendicular to the cross-section defined by $H_{t,i}$ and $W_{t,i}$). The half-height and half-width are taken as the maximum and minimum half-size of the cross-section, respectively. Since pores are in the center of CVs, the length of the two throats in a certain direction is the same ($L_{t1,i} = L_{t2,i}$), $L_{t,i} = (L_{cv,i} - L_{p,i})/2$. The cross-sectional area of the two throats aligned in i-direction is $A_{t1,i} = 4H_{t1,i}W_{t1,i}$ and $A_{t2,i} = 4H_{t2,i}W_{t2,i}$. Whereas the cross-sectional areas of pores perpendicular to each spatial direction are $A_{p,x} = L_{p,y}L_{p,z}$, $A_{p,y} = L_{p,x}L_{p,z}$ and $A_{p,z} = L_{p,x}L_{p,y}$.

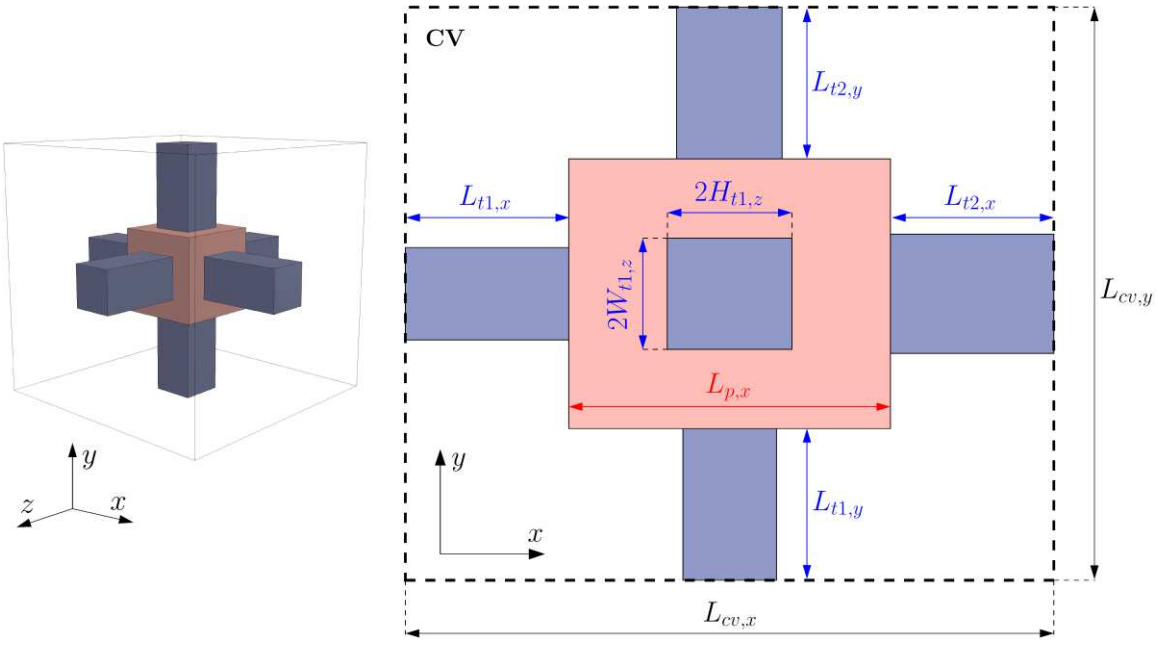

Figure 2. (left) Schematic of the pore and six throats (two in each direction) inside a CV. (right) Geometrical parameters of the structured PN as seen from the *x*-*y* plane (similar considerations apply for other planes).

The generation of the PN in the GDL domain was done using a similar procedure to that presented by Gostick et al. (19). The main steps are described below:

1. A uniform distribution P of $3N$ random numbers is generated in the interval $[P_{min}, P_{max}]$, where P_{min} and P_{max} are the minimum and maximum cumulative probabilities, respectively. The limits are kept close to $P_{min} \approx 0$ and $P_{max} \approx 1$, but manipulated to avoid the inclusion of exceedingly small and large pore sizes that are not representative of the material.

2. The pore sizes L_p corresponding to cumulative probabilities P are determined using the CPSD of the GDL. Note that the CPSD univocally links a cumulative probability P with a pore half-size, $L_p/2$, and vice versa. L_p is then obtained by multiplying by two.

3. N pore sizes are randomly assigned to each direction i ($i = x, y, z$). It is ensured that the maximum pore size in i-direction does not exceed the size of the CV in that direction ($L_{p,i}^{max} < L_{cv,i}$). The pore sizes are first assigned in the through-plane direction (y-direction), and then in the material plane (x and z directions). Subsequently, the vectors with the N pore sizes in each direction i are converted to 3D arrays $L_{p,i}$.

4. The 3D arrays of cumulative probabilities P_i corresponding to the 3D arrays of pore sizes $L_{p,i}$ are determined using the CPSD.

5. Spatial correlations are imparted by applying a convolution filter on x-z slices of the 3D arrays P_i. The kernel used is

$$K = \frac{1}{5}\begin{bmatrix} 0 & 1 & 0 \\ 1 & 1 & 1 \\ 0 & 1 & 0 \end{bmatrix} \quad (1)$$

   As a result, anisotropy is introduced in the PN, reducing the tortuosity of transport pathways in the material plane compared to the through-plane direction (20,21).

6. As shown in Figure 3, the above step has the side effect of converting the initially uniform random distributions P_i into normal ones. Hence, uniform distributions are re-obtained by applying the inverse cumulative distribution function of the normal distributions with the corresponding mean and standard deviation. This step is necessary to ensure that the final PN is composed of a uniform random distribution of cumulative probabilities, so that the pore sizes are not affected by external factors other than the CPSD of the GDL.

7. The pore sizes $L_{p,i}$ corresponding to the uniform distributions of cumulative probabilities P_i are determined according to the CPSD.

8. The length of throats, $L_{t,i}$, and the cross-sectional area of throats, $A_{t,i}$, and pores, $A_{p,i}$, are determined based on the pore sizes, $L_{p,i}$, and the CV sizes, $L_{cv,i}$. In the process, the half-height and half-width of the throats, $H_{t,i}$ and $W_{t,i}$, are taken as the average of the half-sizes, $L_{p,i}/2$, of the two connected pores. This is done to capture the high porosity of GDLs, where pore bodies and throats are not very well defined (22,23).

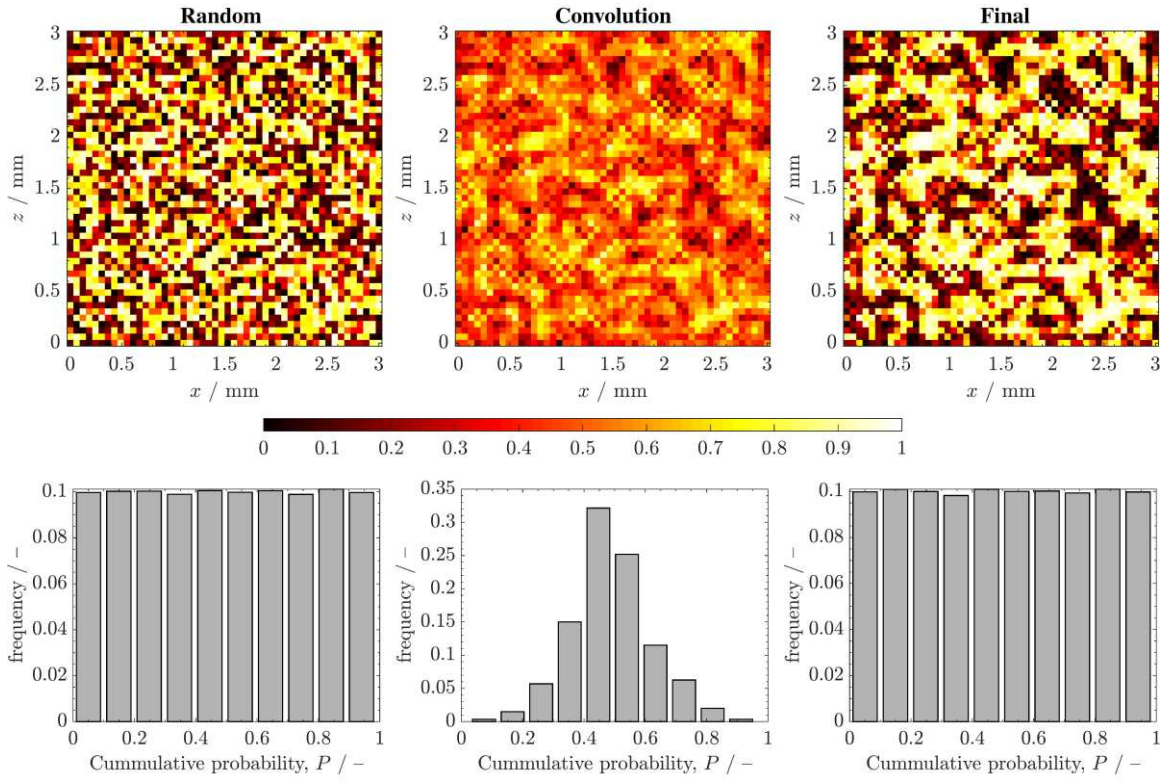

Figure 3. 2D spatial distributions on a x-z slice and histograms of cumulative probabilities $P = \{P_x, P_y, P_z\}$ prescribed initially with a uniform random distribution, after applying the convolution filter, and after the resulting normal distribution is converted back to a uniform distribution (final result).

The resulting PN is shown in Figure 4, which statistically represents the pore space of highly porous, anisotropic GDLs.

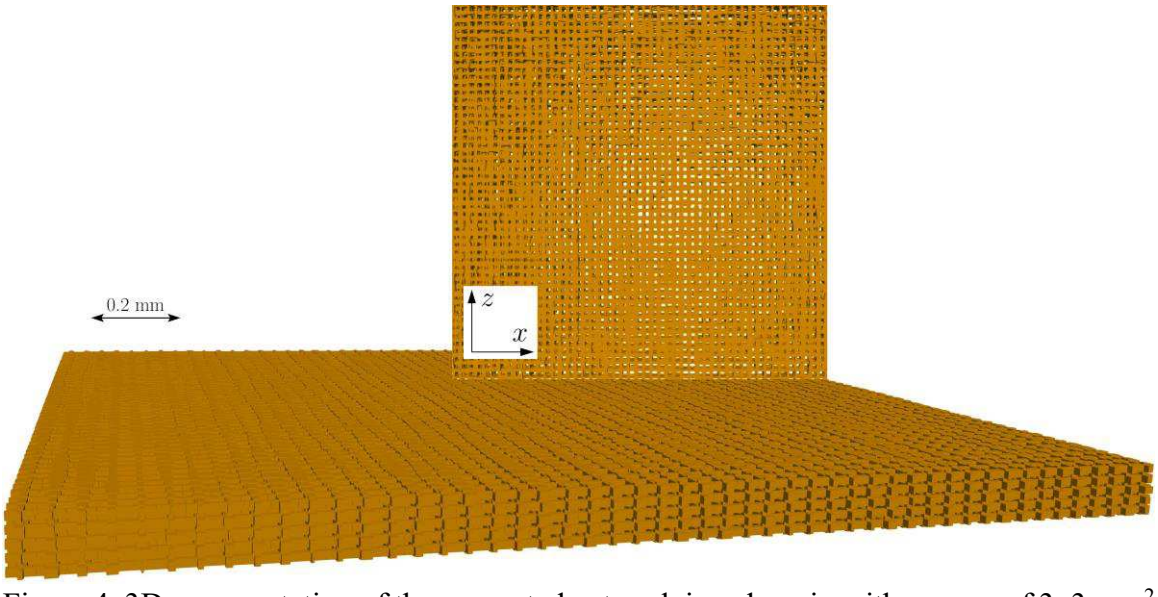

Figure 4. 3D representation of the generated network in a domain with an area of 3x3 mm^2 in the material plane (*x*-*z* plane) and 150 μm in thickness.

Local Effective Transport Properties

Species diffusion and hydraulic convection are modeled in the CV mesh incorporating the microscopic information from the PN. To this end, the local 1D resistances of the structured PN are transformed into local anisotropic effective or equivalent transport properties (effective diffusivity and permeability). As shown in Figure 5, the local effective properties are determined analytically by imposing a concentration or pressure difference, $\Delta C = C_i - C_o$ or $\Delta p = p_i - p_o$, in each direction of interest i ($i = x, y, z$), while imposing a no-flux (or no-flow) boundary condition in the remaining directions (24). This leads to non-zero diagonal components and virtually zero off-diagonal components in the effective diffusivity and permeability tensors, as usually observed in GDLs (9).

For diffusion, the set of equations that govern the diffusive flux in i-direction, j_i, expressed in [mol s^{-1}], in each CV is given by

$$j_{t1,i} = -D\frac{C_i - C_1}{L_{t1,i}}A_{t1,i} \tag{2a}$$

$$j_{p,i} = -D\frac{C_1 - C_2}{L_{p,i}}A_{p,i} \tag{2b}$$

$$j_{t2,i} = -D\frac{C_2 - C_o}{L_{t2,i}}A_{t2,i} \tag{2c}$$

$$j = j_{t1,i} = j_{p,i} = j_{t2,i} \tag{2d}$$

where $A_{p,i}$, $A_{t1,i}$ and $A_{t2,i}$ are the cross-sectional areas perpendicular to i-direction and $L_{t1,i}$, $L_{p,i}$ and $L_{t2,i}$ are the lengths in i-direction of the pore p and throats $t1$ and $t2$ ($L_{t1,i} = L_{t2,i}$), and D is the bulk diffusivity.

The above equations can be combined with the definition of local effective diffusivity, $D_{local,i}^{eff}$, which relates the diffusive flux j with the concentration difference ΔC, i.e.,

$$j = -D_{local,i}^{eff}\frac{C_i - C_o}{2L_{t,i} + L_{p,i}}A_{cv,i} \tag{3}$$

where $A_{cv,i}$ is the cross-sectional area of the CV perpendicular to i-direction. The resulting expression for the normalized effective diffusivity is

$$\frac{D_{local,i}^{eff}}{D} = \frac{\left(\frac{L_{t1,i}}{A_{t1,i}} + \frac{L_{p,i}}{A_{p,i}} + \frac{L_{t2,i}}{A_{t2,i}}\right)^{-1}}{\frac{A_{cv,i}}{2L_{t,i} + L_{p,i}}} \tag{4}$$

This result is the same to that found from linear theory for resistors in series

$$g_{local,i}^{eff,d} = \left(\frac{1}{g_{t1,i}^{d}} + \frac{1}{g_{p,i}^{d}} + \frac{1}{g_{t2,i}^{d}}\right)^{-1} \tag{5}$$

where $g^d = DA/L$ is the diffusive conductivity.

The above averaging procedure can be generalized for the case that there is more than one pore in each CV, so that $L_{cv,x} = L_{cv,z}$ is increased in proportion to the number of pores included. This can reduce the computational cost in simulations on large domains if the number of computational cells per CV and per connector is kept approximately the same.

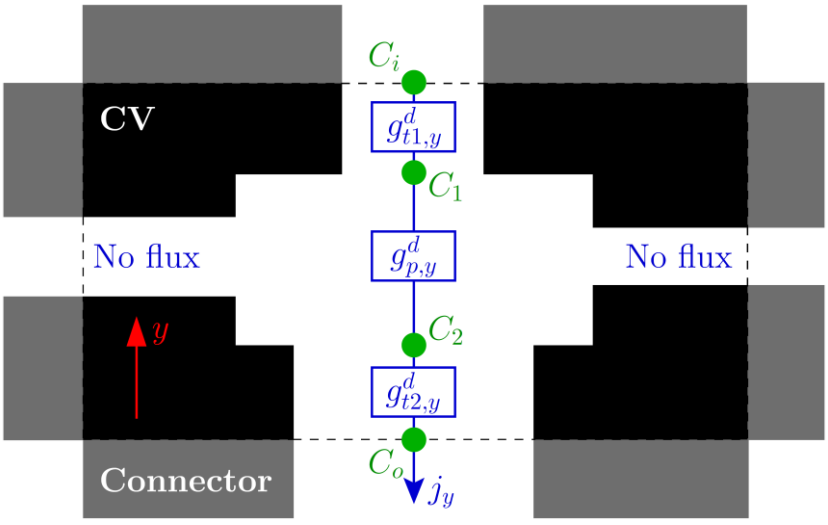

Figure 5. Schematic showing the 1D serial resistor network used for the calculation of the local effective diffusivity, $D^{eff}_{local,y}/D$, in the y-direction. The diffusive conductivities (g^d_y), concentrations (C_i, C_1, C_2 and C_o), and diffusive flux (j_y) through the resistor network are indicated. No-flux boundary conditions are set in the remaining directions. A similar procedure is used for other directions and calculations of local permeability.

Similarly, using Darcy's law, the set of equations that govern the volume flow rate in i-direction, Q_i, expressed in $[\mathrm{m^3 s^{-1}}]$, in each CV is

$$Q_{t1,i} = -\frac{K_{t1,i}}{\mu}\frac{p_i - p_1}{L_{t1,i}}A_{t1,i} \tag{6a}$$

$$Q_{p,i} = -\frac{K_{p,i}}{\mu}\frac{p_1 - p_2}{L_{p,i}}A_{p,i} \tag{6b}$$

$$Q_{t2,i} = -\frac{K_{t2,i}}{\mu}\frac{p_2 - p_o}{L_{t2,i}}A_{t2,i} \tag{6c}$$

$$Q = Q_{t1,i} = Q_{p,i} = Q_{t2,i} \tag{6d}$$

where μ is the dynamic viscosity, and $K_{t1,i}$, $K_{p,i}$ and $K_{t2,i}$ are the permeabilities of the pore and throats $t1$ and $t2$ when the flow is in i-direction. For a rectangular channel, the permeability K_i is given by (25)

$$K_i = \frac{d^2_{h,i}}{48}\left(\frac{\alpha_i + 1}{\alpha_i}\right)^2\left[1 - \frac{192}{\alpha_i}\sum_{n=1}^{\infty}\frac{1}{u_n^5}\tanh\left(u_n\frac{\alpha_i}{2}\right)\right] \tag{7}$$

where $u_n = (2n-1)\pi$, $d_{h,i} = 2\alpha_i(2b_i)/(\alpha_i + 1)$ is the hydraulic diameter, and $\alpha_i = a_i/b_i \geq 1$ is the aspect ratio of the channel, with a_i and b_i the maximum and minimum half-size of the cross-section perpendicular to i-direction, respectively. That is, for throats, $a_i = H_{t,i}$ and $b_i = W_{t,i}$, and for pores, $a_x = \max(L_{p,y}, L_{p,z})$, $a_y = \max(L_{p,x}, L_{p,z})$, $a_z = \max(L_{p,x}, L_{p,y})$, $b_x = \min(L_{p,y}, L_{p,z})$, $b_y = \min(L_{p,x}, L_{p,z})$, $b_z = \min(L_{p,x}, L_{p,y})$. Since the series in (7) is rapidly convergent, 10 terms were used in practice, leading to a relative error of 10^{-6} for $1 < \alpha_i < 20$ (compared to using 10^3 terms).

Equations (6a)-(6d) can be combined with the definition of local effective permeability, $K^{eff}_{local,i}$, which relates the volume flow rate Q with the pressure drop Δp, i.e.,

$$Q = -K_{local,i}^{eff} \frac{p_i - p_o}{2L_{t,i} + L_{p,i}} A_{cv,i}, \tag{8}$$

resulting in the following expression for $K_{local,i}^{eff}$

$$K_{local,i}^{eff} = \frac{\left(\frac{L_{t1,i}}{A_{t1,i}K_{t1,i}} + \frac{L_{p,i}}{A_{p,i}K_{p,i}} + \frac{L_{t2,i}}{A_{t2,i}K_{t2,i}}\right)^{-1}}{\frac{A_{cv,i}}{2L_{t,i} + L_{p,i}}} \tag{9}$$

As for diffusion, the result is equal to that found for hydraulic conductors in series with a conductivity $g^h = KA/L$

$$g_{local,i}^{eff,h} = \left(\frac{1}{g_{t1,i}^h} + \frac{1}{g_{p,i}^h} + \frac{1}{g_{t2,i}^h}\right)^{-1} \tag{10}$$

The effective properties of connectors for both diffusion and convection are taken as the average value of the two connected CVs.

Figure 6 shows the distribution of local effective transport properties in a $1 \times 1\ \text{mm}^2$ sample. As can be seen, less tortuous pathways and higher macroscopic properties prevail in the in-plane direction according to the embedded PN.

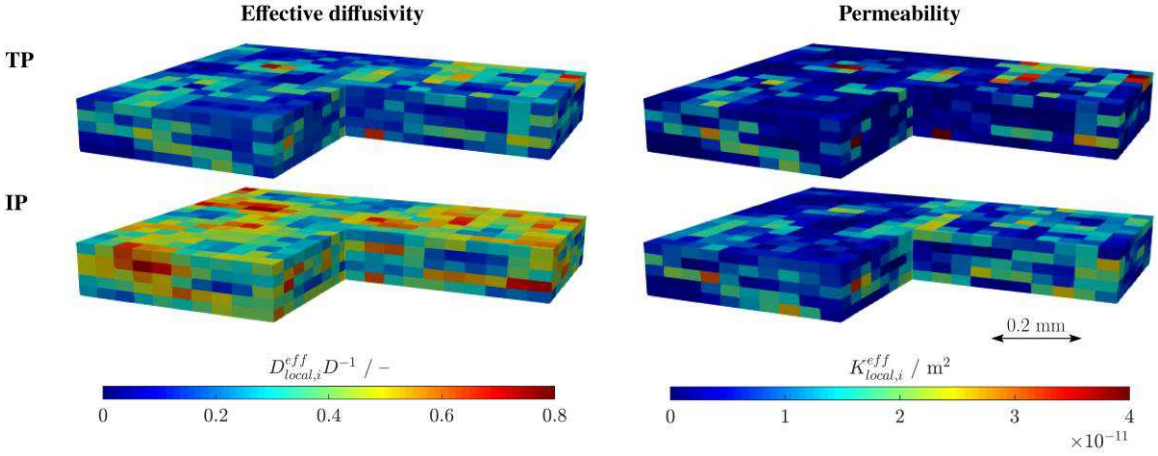

Figure 6. 3D distributions of (left) local normalized effective diffusivity, $D_{local,i}^{eff}/D$, and (right) local effective permeability, $K_{local,i}^{eff}$, in the through-plane ($i = y$) and in-plane ($i = x$) directions. Domain size: $1 \times 1 \times 0.15\ \text{mm}^3$.

Global Effective Transport Properties

The global effective properties are determined from diffusion and hydraulic permeation simulations on the full sample, by imposing a concentration or pressure difference, $\Delta C = C_i - C_o$ or $\Delta p = p_i - p_o$, in the direction of interest i. In both cases, the difference across the sample is set equal to 1 to simplify calculations. Laplace equation is used to model diffusion and convection in the CV mesh at the macroscopic scale

$$\nabla \cdot \boldsymbol{j} = 0 \qquad \Rightarrow \nabla \cdot \left(-\bar{\bar{\boldsymbol{D}}}_{\boldsymbol{local}}^{\boldsymbol{eff}} \nabla C\right) = 0 \tag{11a}$$

$$\nabla \cdot (\rho \boldsymbol{u}) = 0 \Rightarrow \nabla \cdot \left(-\bar{\bar{\boldsymbol{K}}}_{\boldsymbol{local}}^{\boldsymbol{eff}} \nabla p\right) = 0 \tag{11b}$$

The local effective diffusivity and permeability tensors are determined as described in the previous section,

$$\overline{\overline{\boldsymbol{D}}}^{\boldsymbol{eff}}_{\boldsymbol{local}} = \begin{bmatrix} D^{eff}_{local,x} & 0 & 0 \\ 0 & D^{eff}_{local,y} & 0 \\ 0 & 0 & D^{eff}_{local,z} \end{bmatrix} \tag{12a}$$

$$\overline{\overline{\boldsymbol{K}}}^{\boldsymbol{eff}}_{\boldsymbol{local}} = \begin{bmatrix} K^{eff}_{local,x} & 0 & 0 \\ 0 & K^{eff}_{local,y} & 0 \\ 0 & 0 & K^{eff}_{local,z} \end{bmatrix}, \tag{12b}$$

where it has been considered that $D = 1$.

The average diffusive flux and velocity in i-direction ($i = x, y$) computed in the simulations, $j_i = -D^{eff}_{local,i}\partial_i C$ and $u_i = -\left(K^{eff}_{local,i}/\mu\right)\partial_i p$, are used to determine the global effective transport properties

$$\frac{D^{eff}_{global,i}}{D} = \frac{L_{gdl,i}}{V_{gdl}} \int_{V_{gdl}} j_i dV \tag{13a}$$

$$K^{eff}_{global,i} = \frac{L_{gdl,i}\mu}{V_{gdl}} \int_{V_{gdl}} u_i dV \tag{13b}$$

where $L_{gdl,i}$ and V_{gdl} are the length in i-direction and the volume of the GDL sample, respectively. The dynamic viscosity is arbitrarily set equal to that of water at room temperature, $\mu = 10^{-3}$ kg m^{-1} s^{-1}.

Discussion of Results

Two volume-averaged structural properties were used to assess the representativeness of the PN: porosity and pore size. Both quantities were determined by averaging over the entire pore and throat space. The values obtained are $\varepsilon^{avg} = 0.63$ and $L_p^{avg} = 26.5\ \mu$m, which are in good agreement with the data reported by Zenyuk et al. (18) for the GDL examined here ($\varepsilon^{avg} = 0.64$ and $L_p^{avg} = 27\ \mu$m). In addition, the computed global normalized effective diffusivities are $D^{eff}_{global,y}/D = 0.19$ and $D^{eff}_{global,x}/D = 0.38$, which are similar to the experimental data of Flückiger et al. (26). The global permeabilities, $K^{eff}_{global,y} = 4.5 \times 10^{-12}$ m^2 and $K^{eff}_{global,x} = 9 \times 10^{-12}$ m^2, are also in the same range of previous experimental data (9). The good quantitative comparison provide support to the validity of the modeling framework presented here.

Figure 7 shows the computed concentration and pressure distributions corresponding to simulations in the through-plane direction. In both cases, a non-linear decrease of concentration and pressure across the GDL can be seen due to the transport resistance introduced by the pore-throat structure (i.e., the spatially varying effective properties). The changes are sharper for convection due to the stronger sensitivity of local permeability to small pore sizes (i.e., channels with narrow cross-sections). This is different in nature from diffusion, which is mainly influenced by the available pore volume for transport (i.e.,

porosity) (27,28). The ability of the model to capture different modes of transport is important, for example, to examine the effect of cross-flow in PEFCs (29), as well as distributed ohmic and mass transport losses in other electrochemical devices, such as redox flow batteries (30).

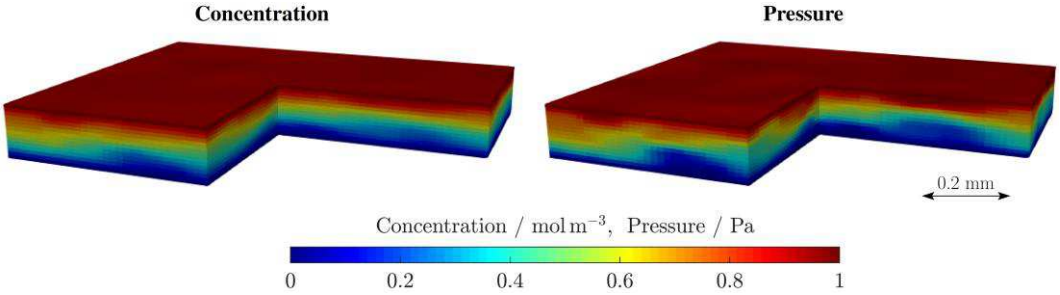

Figure 7. 3D distributions of species concentration and pressure corresponding to simulations of diffusion and convection in the through-plane direction. Simulation parameters: $D = 1$, $C_i = 1$, $C_o = 0$, $p_i = 1$ and $p_o = 0$. Domain size: $1 \times 1 \times 0.15$ mm^3.

Figure 8 shows the 2D distribution of the diffusive flux at the outlet section, as a measure of the heterogeneity of the fluxes from/to the catalyst layer. A significant variation of the diffusive flux is found throughout the GDL, which varies between 200-1800 mol m^{-2} s^{-1} with an average value of 1150 mol m^{-2} s^{-1}. Although overall cell performance is mainly dictated by average fluxes at the cell scale, local variations can affect degradation rates in the catalyst layer (9,31). This aspect should be further examined using a multiphysics model that includes the present formulation. The lower computational cost of network-based models provides an efficient approach to examine the impact of short- and long-range microstructural heterogeneities, along with the spatial inhomogeneities introduced by operating conditions.

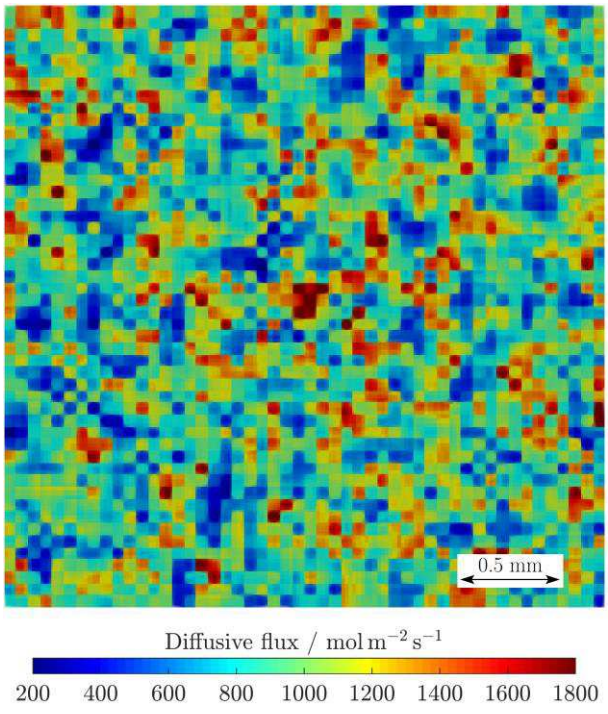

Figure 8. 2D distribution of diffusive flux, j_y, at the outlet surface corresponding to a diffusion simulation in the through-plane direction. Simulation parameters: $D = 1$, $C_i = 1$, and $C_o = 0$. Domain size: $3 \times 3 \times 0.15$ mm^3.

Conclusions

A composite-continuum-network model has been presented to model diffusion and hydraulic convection in thin porous media used in energy conversion and storage electrochemical devices. In particular, the model was applied to model transport in carbon-paper gas diffusion layers (GDLs) used in polymer electrolyte fuel cells (PEFCs). The model incorporates a control volume (CV) mesh at the macroscopic scale, which embeds a structured pore network that is used to determine analytically local effective transport properties in each CV. The CVs in the mesh are connected through differential connectors of negligible volume, which can be used to model invasion percolation of liquid water. The local effective transport properties in the connectors are taken as the mean value of the neighboring CVs.

The model predictions were validated in terms of both global structural parameters and effective transport properties. The average porosity and pore size, as well as anisotropic effective diffusivity and permeability, were found to be in good agreement with previous experimental data. Furthermore, the results showed that the variation of the fluxes from/to the catalyst layer due to microstructural heterogeneities can be significant. The coupled effect of heterogeneous effective transport properties, liquid water blockage, and spatial inhomogeneities introduced by operating conditions on durability should be further examined in future work using a multiphysics model.

Acknowledgments

The model was conceived and partially developed during the stay of P.A. García-Salaberri at LBNL, which was supported by the US-Spain Fulbright commission. P.A. García-Salaberri also thanks the support of the project for young researchers PEM4ENERGYCM-UC3M (Universidad Carlos III de Madrid).

References

1. Y. Wang, K.S. Chen, J. Mishler, S.C. Cho, and X.C. Adroher, *Appl. Energy*, **88**, 981 (2011).
2. S. Zhang, X. Yuan, H. Wang, W. Mérida, H. Zhu, J. Shen, S. Wu, and J. Zhang, *Int. J. Hydrogen Energ.*, **34**, 388 (2009).
3. N. Garland, T. Benjamin, and J.P. Kopasz, DOE Fuel Cell Program: Durability Technical Targets and Testing Protocols, *ECS Trans.*, **11**(1), 923 (2007).
4. J. Zhao and X. Li, *Energ. Convers. Manage.*, **199**, 112022 (2019).
5. R.L. Borup, A. Kusoglu, K.C. Neyerlin, R. Mukundan, R.K. Ahluwalia, D.A. Cullen, K.L. More, A.Z. Weber, and D.J. Myers, *Curr. Opin. Electrochem.*, **21**, 192 (2020).
6. A.Z. Weber, R.L. Borup, R.M. Darling, P.K. Das, T.J. Dursch, W. Gu, D. Harvey, A. Kusoglu, S. Litster, M.M. Mench, R. Mukundan, J.P. Owejan, J.G. Pharoah, M. Secanell, and I.V. Zenyuk, *J. Electrochem. Soc.*, **161**, F1254 (2014).
7. P.A. García-Salaberri, D.G. Sánchez, P. Boillat, M. Vera, and K.A. Friedrich, *J. Power Sources*, **359**, 634 (2017).
8. A. Goshtasbi, P.A. García-Salaberri, J. Chen, K. Talukdar, D.G. Sánchez, and T. Ersal, *J. Electrochem. Soc.*, **166**, F3154 (2019).

9. P.A. García-Salaberri, I.V. Zenyuk, A.D. Shum, G. Hwang, M. Vera, A.Z. Weber, and J.T. Gostick, *Int. J. Heat Mass Tran.*, **127**, 687 (2018).
10. P.A. García-Salaberri, I.V. Zenyuk, G. Hwang, M. Vera, A.Z. Weber, and J.T. Gostick, *Electrochim. Acta*, **295**, 861 (2019).
11. J. Liu, P.A. García-Salaberri, and I.V. Zenyuk, *Transport Porous Med.*, **128**, 363 (2019).
12. J. Hack, P.A. García-Salaberri, M.D.R. Kok, R. Jervis, P.R. Shearing, N. Brandon, and D.J.L. Brett, *J. Electrochem. Soc.*, **167**, 013545 (2020).
13. J. Liu, P.A. García-Salaberri, and I.V. Zenyuk, *J. Electrochem. Soc.*, **167**, 013524 (2020).
14. I.V. Zenyuk, E. Medici, J. Allen, and A.Z. Weber, *Int J. Hydrogen Energ.*, **40**, 16831 (2015).
15. S. Shimpalee, P. Satjaritanun, S. Hirano, N. Tippayawong, and J.W. Weidner, *J. Electrochem. Soc.*, **166**, F534 (2019).
16. T. Jahnke, G. Futter, A. Latz, T. Malkow, G. Papakonstantinou, G. Tsotridis, P. Schott, M. Gérard, M. Quinaud, M. Quiroga, A.A. Franco, K. Malek, F. Calle-Vallejo, R. Ferreira de Morais, T. Kerber, P. Sautet, D. Loffreda, S. Strahl, M. Serra, P. Polverino, C. Pianese, M. Mayur, W.G. Bessler, and C. Kompis, *J. Power Sources*, **304**, 207 (2016).
17. P.A. García-Salaberri, M. Vera, and R. Zaera, *Int J. Hydrogen Energ.,* **36**, 11856 (2011).
18. I.V. Zenyuk, D.Y. Parkinson, L.G. Connolly, and A.Z. Weber, *J. Power Sources*, **328**, 364 (2016).
19. J.T. Gostick, M.A. Ioannidis, M.W. Fowler, and M.D. Pritzker, *J. Power Sources*, **173**, 277 (2007).
20. P.A. García-Salaberri, G. Hwang, M. Vera, A.Z. Weber, and J.T. Gostick, *Int. J. Heat Mass Tran.*, **86**, 319 (2015).
21. P.A. García-Salaberri, J.T. Gostick, G. Hwang, A.Z. Weber, and M. Vera, *J. Power Sources*, **296**, 440 (2015).
22. J.T. Gostick, *Phys. Rev. E*, **96**, 023307 (2017).
23. T. Agaesse, A. Lamibrac, F.N. Büchi, J. Pauchet, and M. Prat, *J. Power Sources*, **331**, 462 (2016).
24. R. Guibert, P. Horgue, G. Debenest, and M. Quintard, *Math. Geosci.*, **48**, 329 (2016).
25. W. Rybinski and J. Mikielewicz, *Arch. Thermodyn.*, **35**, 29 (2014).
26. R. Flückiger, S.A. Freunberger, D. Kramer, A. Wokaun, G.G. Scherer, and F.N. Büchi, *Electrichim. Acta*, **54**, 551 (2008).
27. T. Rosén, J. Eller, J. Kang, N.I. Prasianakis, J. Mantzaras, and F.N. Büchi, *J. Electrochem. Soc.*, **159**, F536 (2012).
28. L. Holzer, O. Pecho, J. Schumacher, Ph. Marmet, O. Stenzel, F.N. Büchi, A. Lamibrac, and B. Münch, *Electrochim. Acta*, **227**, 419 (2017).
29. A.D. Santamaria, M.K. Becton, N.J. Cooper, A.Z. Weber, and J.W. Park, *J. Power Sources*, **293**, 162 (2015).
30. A.M. Pezeshki, R.L. Sacci, F.M. Delnick, D.S. Aaron, and M.M. Mench, *Electrochim. Acta*, **229**, 261 (2017).
31. P.A. García-Salaberri, J.T. Gostick, I.V. Zenyuk, G. Hwang, M. Vera, and A.Z. Weber, *ECS Trans.*, **80**(8), 133 (2017).